IET Renewable Power Generation
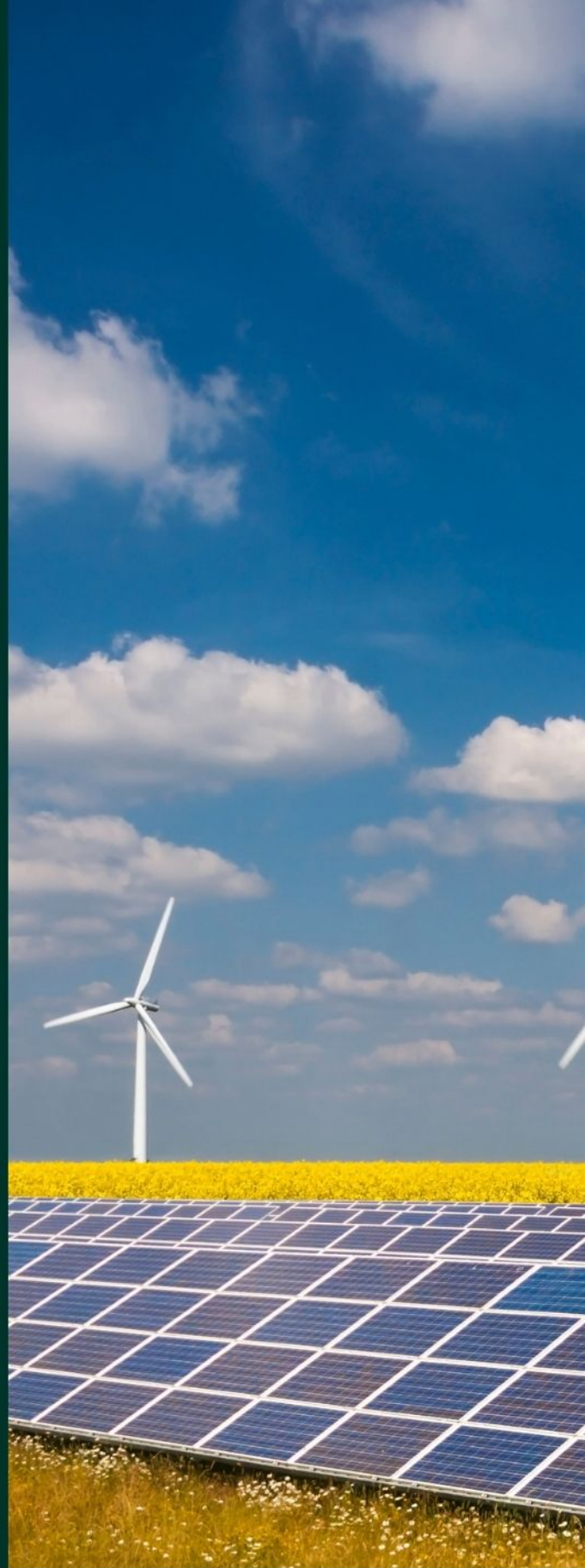
The Institution of Engineering and Technology WILEY

ORIGINAL RESEARCH PAPER

Hierarchical control and emulation of a wave energy hyperbaric converter

Isaac R. Machado[1] | Paula B. Garcia-Rosa[2] | Edson H. Watanabe[3]

[1] Postgraduate Program in Electrical and Computer Engineering - PPGEEC, Federal University of Ceará - UFC, Sobral, Brazil

[2] SINTEF Energy Research, Trondheim, Norway

[3] Department of Electrical Engineering, COPPE/Federal University of Rio de Janeiro, Brazil

Correspondence

Isaac R. Machado, Postgraduate Program in Electrical and Computer Engineering, Federal University of Ceará, Sobral, Brazil.
Email: isaacmachado@ufc.br

Abstract

Wave energy emulators provide an option to extend studies of wave energy converters (WECs) in an electric power laboratory facility and to evaluate the performance of controllers in an experimental set-up. In addition, the integration of control strategies in different steps of the energy conversion process is an important step to improve the WEC overall behaviour that has not yet been widely discussed. This paper proposes a real-time emulator and a hierarchical control scheme for a hyperbaric WEC consisting of floating bodies, hydropneumatic storage system (HSS), hydraulic turbine, and doubly fed induction generator (DFIG). The proposed emulator is based on a typical electric power laboratory facility, where a numerical model reproduces the dynamics of the wet subsystem and a hardware is the WEC electrical subsystem. Thereby, a squirrel-cage induction motor (SCIM) is coupled shaft-to-shaft with the DFIG. The SCIM reproduces the characteristics of torque and speed that would be observed in the real system, and then, the DFIG is subjected to a primary drive with same dynamic characteristics of the real plant. The hierarchical control integrates the generator and HSS controllers considering the optimal operating pressure for local sea state conditions. Experimental results illustrate the performance of the emulator and controllers.

1 | INTRODUCTION

Prior to the deployment of full-scale prototypes, wave energy converters (WECs) are commonly studied by numerical simulations and experimental tests by means of small-scale models at wave basin facilities. Furthermore, a number of studies have investigated the design and implementation of control systems for WECs, in order to improve the energy absorption or other performance factors [1–8]. Such studies are usually carried out with numerical models, but a few control schemes have been tested at wave tank scenarios [9–13].

However, the access to wave basin facilities can be limited to short periods of time, and the tests performed at these facilities commonly only account for the hydrodynamics and the mechanical characteristics of the system. In contrast, the development of WEC emulation systems in typical electric power laboratory settings can represent a feasible option for carrying out experimental studies, where electrical subsystems are conveniently assembled. In such emulation systems, the hardware is the electrical subsystem of the WEC and a numerical model reproduces the dynamics of the wet subsystem. Wave energy emulators have been proposed for direct-drive WECs [14, 15], oscillating water column plants [16], a point absorber with electromechanical power take-off (PTO) system [17], and a flap-type WEC [18].

This paper proposes an emulator for a wave energy hyperbaric converter developed by COPPE/Federal University of Rio de Janeiro, Brazil [19]. The hyperbaric WEC can be divided into two main power conversion units: the primary conversion unit (PCU), and the secondary conversion unit (SCU), as illustrated in Figure 1. The PCU comprises a hydraulic PTO system, which consists of floating bodies, hydraulic pumps, a two-stage accumulator connected to a hyperbaric chamber, and a Pelton turbine. The SCU comprises the equipment responsible for the electromechanical energy conversion: an electric generator and power electronic converters required for the generator's voltage and frequency control, which allow the generator to operate at variable speeds by decoupling the rotor speed from the electrical
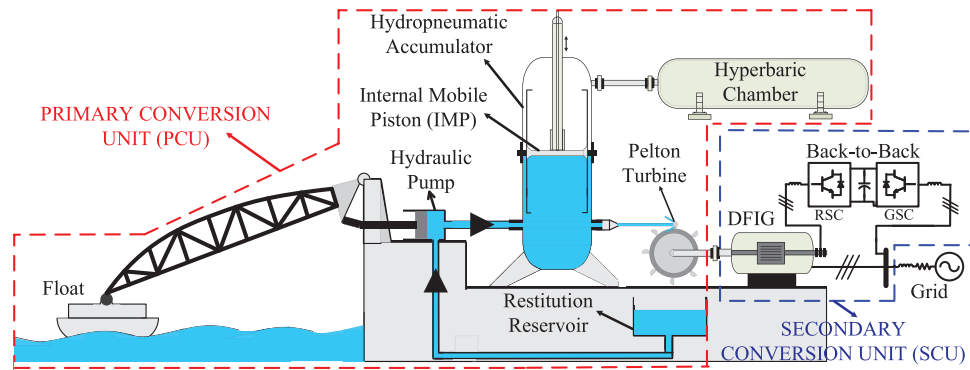
FIGURE 1 Schematic of the hyperbaric WEC

frequency of the grid. The working principle of the WEC is based on the body motion, which drives hydraulic pumps through mechanical arms and displaces water to the accumulator. The accumulator and the hyperbaric chamber represent a hydropneumatic storage system (HSS), responsible for storing the captured energy in the form of compressed air, and releasing a pressurized water flow to drive the hydraulic turbine. In the configuration adopted in this study, the turbine drives a doubly fed induction generator (DFIG).

Other studies related to the hyperbaric WEC have focused on small-scale model studies [20], dynamic wave-to-wire modelling [21], optimizing the wave energy absorption [22], verifying the impact of the storage system on the quality of the generated power for different configurations of the SCU [21][23], and distributed generation applications [24]. In contrast to [23], where the DFIG is controlled by the mechanical speed, this work presents a different control strategy for the DFIG, which is controlled by the active power. This represents a significant difference in terms of power quality, as with active power control, the inertia of the rotor filters the wave power oscillations, and then, the electrical power exhibits a certain level of filtering when compared to the mechanical power that has not been observed with the DFIG controlled by speed. A full-scale prototype with two floating bodies was installed in the Pecém port, in the state of Ceará in Brazil [25]. Nonetheless, the integration of control strategies applied to the PCU and to the SCU is an important step in the development of the hyperbaric WEC that has not been developed. In addition, the emulation system proposed in this work allows for experimental verification of the control system, which has not been performed in previous studies.

Overall, most papers on wave energy control focus on optimizing the WEC primary energy conversion, for example [3–7]. Although many studies discuss wave-to-wire models, for example [16, 21, 26], control strategies aiming at optimizing the wave-to-wire energy system or integrating the subsystems to improve the WEC performance, have not been widely discussed, especially for WECs with hydraulic PTOs. This paper propose a hierarchical control scheme to integrate the HSS and generator controllers, and then, improve the overall behaviour of the hyperbaric converter. The HSS control considers the optimal

pressure of the system in order to improve the wave energy absorption.

The performance of the hierarchical control is verified in an experimental set-up, where the proposed emulator represents the behaviour of the PCU subsystems through a numerical model and a squirrel-cage induction motor (SCIM) reproduces the mechanical speed imposed to the DFIG. Then, the SCIM is driven by a voltage source converter (VSC) emulating the Pelton turbine. The SCIM is coupled shaft-to-shaft to the electric generator, which is connected to the local power grid through the power electronic interface.

2 | NUMERICAL MODELS OF THE EMULATOR

This section describes the numerical models of the incident waves, and the PCU of the hyperbaric WEC.

2.1 | Incident waves

In deep water, wind-generated waves can be categorized as a Gaussian stochastic process, and are usually approximated as a superposition of a number of sinusoidal waves. Such waves are characterized by a wave spectrum $S(\omega)$ [27]. Here, we assume the floating bodies are subjected to polychromatic waves characterized by the Bretschneider spectrum, which can be expressed as

$$S(\omega) = \frac{A_w}{\omega^5} \exp\left(-\frac{B_w}{\omega^4}\right), \tag{1}$$

with

$$A_w = 172.5 \frac{H_s^2}{T_{av}^4} \quad \text{and} \quad B_w = \frac{691}{T_{av}^4}, \tag{2}$$

where ω is the wave angular frequency, H_s is the significant wave height, and T_{av} is the average period of the wave spectrum.

The polychromatic waves are calculated as

$$\zeta(t) = \sum_{i=1}^{m} a_i \cos(\omega_i t + \phi_i),\qquad(3)$$

where a_i is the amplitude of the i-th wave component,

$$a_i = \sqrt{2S(\omega_i)\,\omega_i},\qquad(4)$$

ω_i and ϕ_i are, respectively, the angular frequency and random phase of the i-th wave component.

2.2 | Pumping modules

The motion of the floating bodies and hydraulic pumps describes the model of the pumping modules [21]. Here, we assume linear hydrodynamic theory and heave oscillatory motion of the body. Thus, the body motion is given by

$$m\ddot{x}(t) + \int_0^t h_r(t-\tau)\dot{x}(\tau)\,d\tau + K_e x(t) = f_e(t) + f_p(t),\qquad(5)$$

where the kernel of the convolution term $h_r(t-\tau)$ is known as the fluid memory term [28], given by

$$h_r(t-\tau) = \frac{2}{\pi}\int_0^\infty R_r(\omega)\cos\left[\omega(t-\tau)\right]d\omega,\qquad(6)$$

$m = M + m_r(\infty)$, x is the position of the body, M is the mass of the body, $m_r(\infty)$ is the infinite-frequency added mass coefficient, $R_r(\omega)$ is the radiation damping coefficient, and K_e is the buoyancy stiffness of the floating body.

The external forces applied to the floating body are the wave excitation force f_e, and the PTO force f_p. For polychromatic waves (3),

$$f_e(t) = \sum_{i=1}^{m} F_{ei}\cos(\omega_i t + \phi_i),\qquad(7)$$

where F_{ei} is the excitation force coefficient of the i-th component. For axisymmetric bodies and a sinusoidal wave with amplitude a_i and frequency ω_i [29],

$$F_{ei}(\omega_i) = \left(\frac{2\rho g^2 a_i^2 R_r(\omega_i)}{\omega_i k_i}\right)^{1/2},\qquad(8)$$

where ρ is the water density, g is the gravity acceleration and k_i is the wavenumber.

The PTO force (f_p) represents the force applied by the pump to the body. Two stages are defined according to the body motion: (a) the high-pressure stage occurs during the downward motion of the body, when water is injected into the accumulator; (b) the low-pressure stage occurs during the upward motion
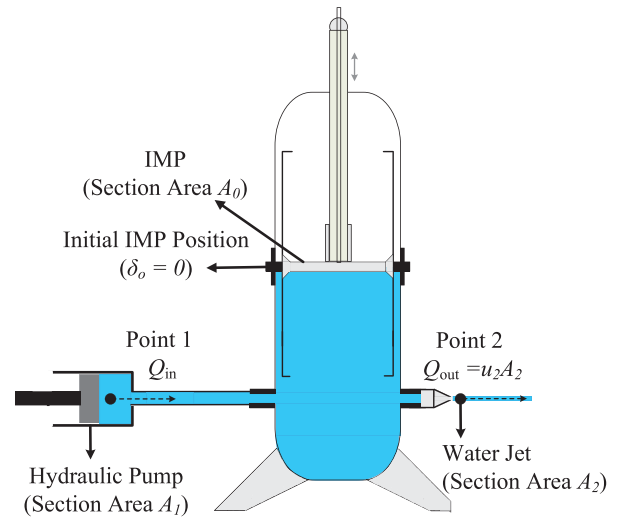

FIGURE 2 Schematic of the accumulator and variables of the HSS model

of the body, when the pump is filled with water. Thus, the PTO force is defined as [20]

$$f_p(t) = \begin{cases} 0, & \dot{x}(t) \geq 0, \\ A_1 p_1(t), & \dot{x}(t) < 0, \end{cases}\qquad(9)$$

where A_1 is the cross-sectional area of the hydraulic pump and p_1 is the hydraulic pressure of the HSS.

The water flow into the accumulator for the n-th floating body is calculated by

$$Q_{a,n}(t) = \begin{cases} 0, & \dot{x}_n(t) \geq 0, \\ A_1\dot{x}_n(t), & \dot{x}_n(t) < 0, \end{cases}\qquad(10)$$

where x_n is the position of the n-th body, and the total flow of water for k floating bodies is given by

$$Q_{in}(t) = \sum_{n=1}^{k} Q_{a,n}(t).\qquad(11)$$

2.3 | Hydropneumatic storage system

The HSS consists of the accumulator and the hyperbaric chamber. The hyperbaric chamber is filled with pressurized air, and is responsible for smoothing the pressure fluctuations in the HSS [21]. Figure 2 illustrates the variables of the HSS model, and the internal section of the accumulator, which is divided into air and water separated by a piston.

By applying the Bernoulli's equation to points 1 and 2 of Figure 2, the velocity of the water jet at point 2 is calculated as

$$u_2(t) = \left(u_1^2(t) + \frac{2}{\rho}(p_1(t) - p_2)\right)^{1/2},\qquad(12)$$

where the variables p and u represent, respectively, the pressures and the velocities of water jets. The pressure at point 2 (p_2) is the atmospheric pressure (1 atm or 10^5 N/m^2) and the HSS internal pressure, $p_1(t)$, is a function of the internal mobile piston (IMP) position, $\delta(t)$.

Here, we assume that the gas compression/expansion process in the HSS is an isothermal process. Thus, $p_1(t)$ is obtained by the equation of ideal gases,

$$p_1(t) = \frac{p_0 \mathcal{V}_0}{\mathcal{V}_1(t)} = \left(\frac{\mathcal{V}_0}{\mathcal{V}_0 - \delta(t) A_0} \right) p_0 , \qquad (13)$$

where p_0 and $\mathcal{V}_0$ represent, respectively, the initial hydraulic pressure and the initial volume of gas in the hyperbaric chamber, and A_0 is the accumulator cross-sectional area. $\mathcal{V}_1$ and p_1 represent, respectively, the volume of gas after compression (or expansion) and the pressure. From (12) and (13),

$$u_2(t) = \left(u_1^2(t) + \frac{2}{\rho} \left(\frac{p_0 \mathcal{V}_0}{\mathcal{V}_0 - \delta(t) A_0} - p_2 \right) \right)^{1/2} . \qquad (14)$$

In (14), the velocity of the water jet (u_2) is a function of the piston position (δ), the pressure, and the velocity u_1. However, u_2 is much larger than u_1, hence u_2 is mainly influenced by the internal IMP position term, and u_1 can be neglected. Section 5 shows that, by controlling the IMP position, an indirect control of p_1 and u_2 is obtained.

The volume of water inside the accumulator is governed by the law of conservation of mass. Thus, the IMP position can be expressed as

$$\delta(t) = \frac{1}{A_0} \int Q_{in}(t) dt - \frac{A_2}{A_0} \int u_2(t) dt + \delta_0 , \qquad (15)$$

where Q_{in} is the HSS input water flow, δ_0 is the IMP initial position, and A_2 is the cross-sectional area of the water jet at point 2 (Figure 2). Additionally, the HSS output water flow Q_{out} is calculated as the product of the velocity u_2 and area A_2.

2.4 | Pelton turbine

The wheel (or runner) of a Pelton turbine consists of a number of buckets. The incident water flow (from the HSS) strikes the buckets, imposing momentum and causing the rotation of the turbine. The buckets are shaped in such a way as to divide the flow in half. From the angular momentum equation for a fixed control volume, the turbine mechanical torque can be calculated as in [30]:

$$T_m(t) = R(u_2(t) - \omega_m R)(1 - cos\theta)\rho \, Q_{out}(t) , \qquad (16)$$

where ω_m is the turbine angular speed, R is the radius of the wheel, and θ is the water flow exit angle. Thus, the turbine mechanical power is given by

$$P_m(t) = R\omega_m(u_2(t) - \omega_m R)(1 - cos\theta)\rho A_2(t) u_2(t) , \qquad (17)$$

where $A_2(t)$ is the flow area modified by the position control of the IMP, which is described in Section 3.1. Assuming u_2 and A_2 are constant, the maximum mechanical power is obtained when

$$\omega_m = \omega_{m\_opt} = \frac{u_2}{2R} . \qquad (18)$$

3 | CONTROL STRATEGIES

In order to improve the overall behaviour of the WEC, the PCU and SCU controllers must act in an integrated way. Here, a hierarchical control scheme that integrates both the HSS and the generator controllers is proposed. Figure 3 illustrates the HSS and DFIG control strategies, where the active stator power reference P_{s_ref} for the DFIG control is calculated from the HSS control, and the control loop for the emulation of the turbine mechanical speed is calculated by using the SCIM, which will be further explained in Section 4.1.

3.1 | HSS control

The HSS control is based on the position control of the internal piston in the accumulator. The control objective is to maintain the IMP position within an average of the desired position δ_{ref}. To improve the wave energy absorption, the desired position is calculated to keep the HSS pressure around the optimum value, which is given by [22]

$$p_{1\_opt} = \frac{\pi F_e(\omega)}{4 A_1} , \qquad (19)$$

for regular waves. Then, from (13)

$$\delta_{ref} = \frac{\mathcal{V}_0}{A_0} \left(1 - \frac{p_0}{p_{1_{opt}}} \right) . \qquad (20)$$

Notice that it would not be feasible to keep the IMP in a constant position, as the HSS would lose its main function, that is to filter fast oscillations in the power. In such a case, all intermittent wave power would be transferred to the turbine. Thus, the IMP should move around an average position within certain limits.

A proportional-integral (PI) controller is adopted for the feedback loop control of the piston position, where a low-pass filter with time constant τ_1 is included to smooth the error $\varepsilon = \delta - \delta_{ref}$, as shown in Figure 3. The filter time constant is adjusted to obtain proper filtering of the instantaneous wave power; it can be adjusted, for example to filter oscillations related to the average period of the wave spectrum (T_{av}).

Notice that by using the pressure p_{1_opt}, (19) relates the HSS control to an optimal hydrodynamic performance of the floating body. To improve the wave energy absorption on an hourly basis, the HSS pressure should be adjusted according to local sea states [22]. Therefore, the reference value for the IMP position (20) can be set every 3 or 4 h according to the duration of local
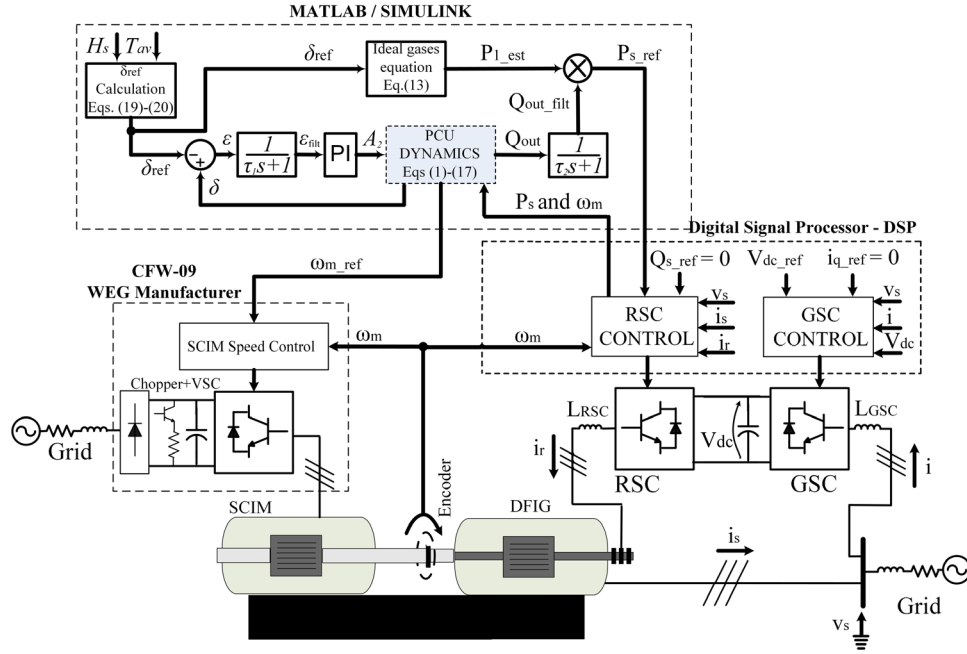
FIGURE 3 WEC control strategies

sea states and using the wave spectrum parameters T_{av} and H_s. This is done by assuming the wave frequency as $\omega := 2\pi/T_{av}$ and amplitude as $a := H_s/2$ in (19) and (8).

3.2 | DFIG control

The stator flux-oriented control strategy is adopted for the DFIG control [31]. In such a way, the stator is connected directly to the grid and the rotor is fed by a back-to-back converter. The grid side converter (GSC) regulates the DC link voltage, and the rotor side converter (RSC) regulates the stator active and reactive powers (P_s and Q_s) based on a field-oriented control algorithm as presented in [32–34]. In this configuration where the DFIG active power is controlled, the rotor speed oscillates around the optimum value calculated as (18) for impulse turbines. Then, the inertia of the rotor further filters the wave power oscillations after the first steps of energy conversion.

The setpoints for the GSC control (V_{dc_ref}, i_{q_ref}) and RSC control (Q_{s_ref}, P_{s_ref}) are, respectively, set as

$$V_{dc\_ref} = 400, \tag{21}$$

$$i_{q\_ref} = 0, \tag{22}$$

$$Q_{s\_ref} = 0, \tag{23}$$

$$P_{s\_ref} = \eta_{turb}\left(Q_{out\_filt}(t)\, p_{1\_est}(t)\right), \tag{24}$$

where V_{dc_ref} is the DC bus voltage reference in volts, i_{q_ref} is the GSC quadrature current in amperes, and P_{s_ref}, Q_{s_ref} are the

control references for the stator active power and stator reactive power, respectively. In this study, the DFIG stator flux-oriented control is associated with the HSS control as indicated in (24), where η_{turb} is the turbine efficiency, $Q_{out\_filt}(t)$ is the filtered output water flow, and $p_{1\_est}(t)$ is given by (13) with $\delta(t) = \delta_{ref}$, as illustrated in Figure 3. Notice that the variables p_1 and Q_{out} are not used in (24) to avoid fast oscillations interfering with the DFIG control dynamics. Such an approach can be performed because the hydraulic system dynamics is much slower than the generator dynamics.

The reference for the stator reactive power is set to zero for all tests implemented, as indicated in (23). Furthermore, the reactive current reference of the RSC control is also set to zero (22) and, thus, a unitary power factor at the point of common coupling (PCC) is obtained.

3.2.1 | GSC control

Figure 4 illustrates the GSC control scheme [34], with the following measured parameters: PCC voltages V_s (V_{sa}, V_{sb}, V_{sc}), GSC currents i (i_a, i_b, i_c) and DC bus voltage (V_{dc}). A PI voltage controller and a PI current controller are used in such a scheme. The use of a phase looked loop (PLL) enables tracking of the PCC voltage vector position, represented by θ_{pll}. Thus, the GSC active and reactive powers are independently controlled through the direct-axis (i_d) and quadrature (i_q) current control loops [32, 33].

Notice that the DFIG model may be simplified if the following assumptions are considered by applying field-oriented control [35, 36]: (i) the stator flux is totally aligned with the d-axis; (ii) the stator voltage vector has a single component in the q-axis ($v_{sd} = 0$). Furthermore, considering that the voltage drop on the
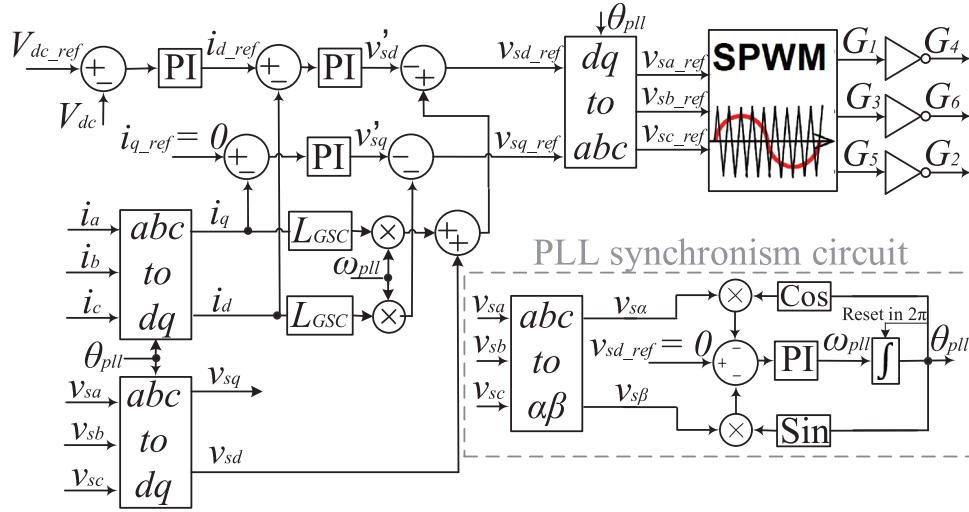
FIGURE 4 GSC control scheme

stator resistance may be neglected, the stator currents are given by [35]

$$i_{sd} = \frac{1}{L_s\omega_s}v_{sq} - \frac{L_m}{L_s}i_{rd}, \qquad (25)$$

$$i_{sq} = -\frac{L_m}{L_s}i_{rq}, \qquad (26)$$

where i_{rd}, i_{rq}, i_{sd} and i_{sq} are machine currents in the dq reference frame. Subscripts r and s correspond to, respectively, rotor and stator quantities, and subscripts d and q correspond to, respectively, direct- and quadrature- axis quantities. L_m, L_s and ω_s are, respectively, the magnetization inductance, the stator self-inductance and the stator angular frequency.

Thus, the stator active and reactive powers are, respectively,

$$P_s = v_{sq}i_{sq}, \quad Q_s = -v_{sq}i_{sd}. \qquad (27)$$

From (25) and (26), it can be noted that when the DFIG operates connected to a fixed voltage bar and the stator flux-oriented control is applied, the rotor and stator currents are directly proportional, and the generator has current source characteristics. Then, (27) can be rewritten as:

$$P_s = -\frac{L_m}{L_s}v_{sq}i_{rq}, \qquad (28)$$

$$Q_s = -\frac{v_{sq}^2}{\omega_s L_s} + \frac{L_m}{L_s}v_{sq}i_{rd}. \qquad (29)$$

Equations (28) and (29) show that it is possible to adjust the stator active (P_s) and reactive powers (Q_s) by controlling, respectively, the q-axis rotor current (i_{rq}) and d-axis rotor current (i_{rd}). The first part of (29) is the reactive power required for the DFIG magnetization. The DFIG magnetization can be performed by either the stator or the rotor side.

3.2.2 | RSC control

Figure 5 illustrates the RSC control scheme [34]. Assuming that the stator resistance is negligible when compared to the inductive reactance, an estimation of the stator flux position (θ_s) is obtained from the PCC voltage vector position, which is obtained from the PLL (θ_{pll}). Thus, the stator flux vector position referred to the rotor (θ_{slip}) is determined by subtracting θ_s from the measured rotor position (θ_r). θ_{slip} is used in all Park transformations for RSC control. Similar to the GSC control, the RSC control also uses two current control loops (dq reference frames) acting in parallel. The control loops of the d-axis rotor current, and the q-axis rotor current, are employed to adjust the reactive and active stator powers, respectively, as indicated in (28) and (29). PI power and current controllers are used in the RSC control scheme. Parameters σ, L_r, and I_{ms} used in the decoupling terms calculation (Figure 5) are, respectively, the total leakage machine factor, rotor self-inductance, and nominal magnetizing current.

4 | EMULATOR DESIGN

Figure 6 illustrates the schematic of the hyperbaric WEC emulator. The system consists of a desktop computer, a vector controlled squirrel-cage induction motor (SCIM) to reproduce the mechanical speed calculated by the numerical model, a wound rotor induction machine (DFIG), back-to-back VSC converters, a digital signal processor (DSP) for the implementation of the generator control (GSC and RSC), voltage and current sensors, conditioning circuits for the analogue signals, and an analogue interface card connected to the PCI slot.

4.1 | Emulation of the mechanical speed by using the SCIM

The DFIG is coupled shaft-to-shaft with the SCIM. In this way, the SCIM imposes torque and speed to the DFIG by emulating
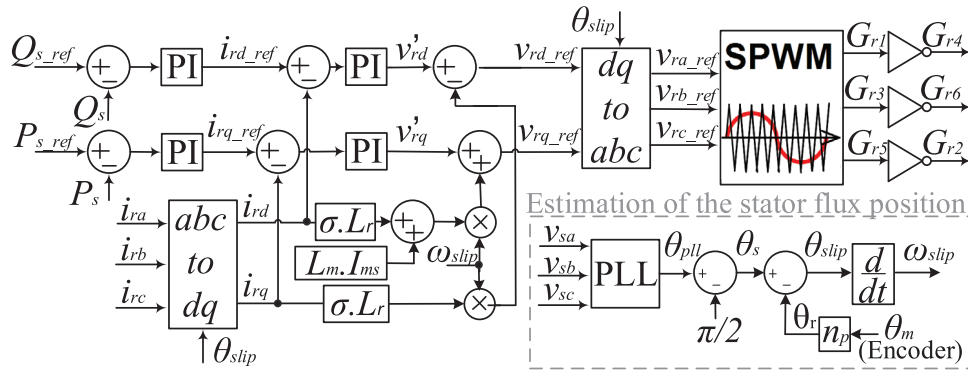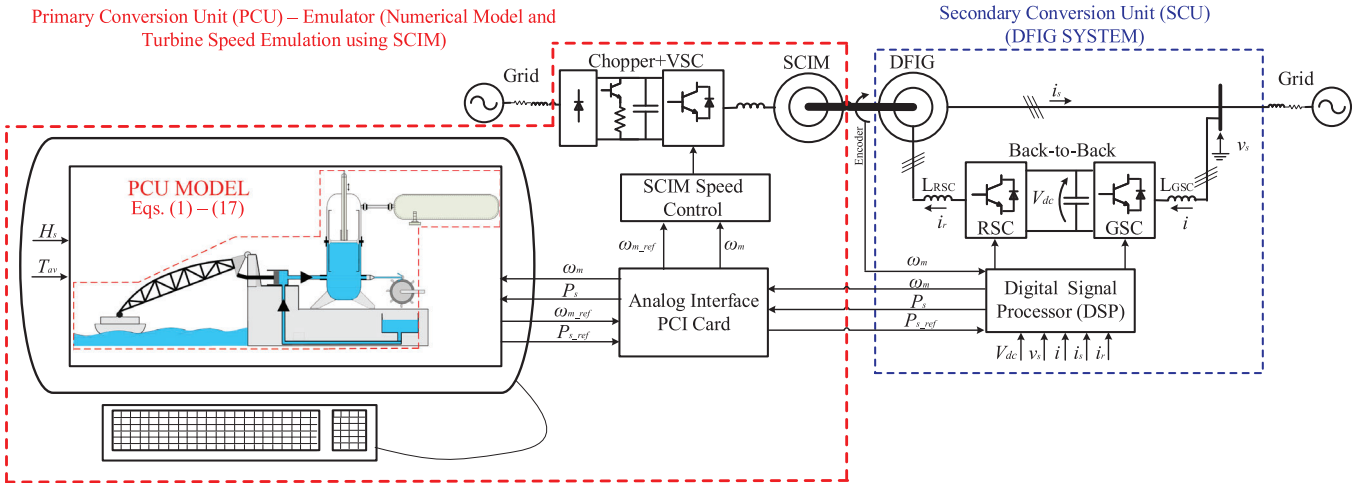
FIGURE 5 RSC control scheme

FIGURE 6 Schematic of the proposed hyperbaric WEC emulator

the PCU behaviour. For a given sea state, after the first energy conversion steps, the mechanical power (P_m) is provided at the turbine-generator shaft. The mechanical power and the electrical power (P_e) are used to solve the following differential equation, which represents the rotational motion of the machine in per unit (p.u.),

$$P_m - P_e = 2H\omega_{m\_ref} \frac{d\omega_{m\_ref}}{dt}, \quad (30)$$

where H is the total rotor inertia constant in seconds, ω_{m_ref} is the machine angular speed reference that is sent to the VSC control, and P_e is estimated as

$$P_e = P_s(1 - S) = P_s \left(1 - \frac{\omega_s - n_p \omega_m}{\omega_s}\right), \quad (31)$$

where S is the slip of the machine, n_p is the number of pole pairs, P_s is the measured active power, and ω_m is the measured angular speed. Notice that P_m and P_e are in p.u in (30) and PCU base values are considered. Thus, the inertia constant H is referred to the PCU side.

The mechanical speed is emulated in real-time by means of a standard SCIM drive converter, which implements the vector speed control through a PI algorithm. Particularly, the developed emulator reproduces the mechanical speed similar to what would be observed in the real plant, and imposes the speed to the generator. The advantage of such approach is the representation of the energy storage equipment (HSS system and rotor moment of inertia) in a simulation environment. Thereby, different configurations and storage capacities can be easily emulated and evaluated together with the experimental implementation of the SCU. Other studies, see, for example [16], reproduce the mechanical torque generated in a turbine shaft.

4.2 | Numerical model

The PCU behaviour is reproduced from the mathematical models (1)–(17) including the HSS control, and the models associated with the mechanical speed emulation (30)–(31). Furthermore, the control reference P_{s_ref} is obtained from (24) and sent to DSP, where the stator flux-oriented control is implemented. The numerical model is implemented on the Matlab/Simulink
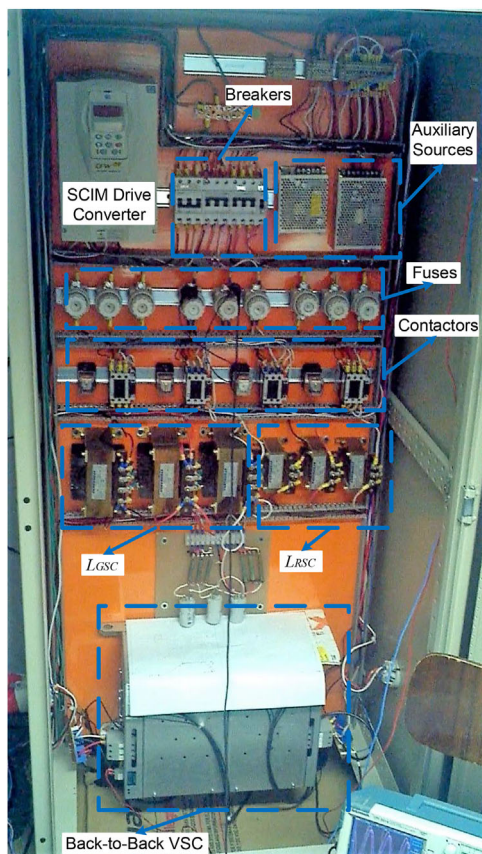
FIGURE 7 Schematic of the numerical model of a WEC with one pumping module

platform in a desktop computer. Figure 7 illustrates a schematic of the numerical model.

In the pumping modules, the floating bodies are vertical cylinders with mass $M = 17 \times 10^3$ kg, where the hydrodynamic data were computed by the boundary element solver WAMIT [37]. In the implemented mathematical model, the equation of motion (5) is represented as the transfer function

$$H_b(s) = \frac{s}{ms^2 + sH_r(s) + K_e},\tag{32}$$

where the model inputs are the external forces (f_e and f_p), the output is the body velocity, and H_r is a transfer function that represents an approximation of the fluid-memory term in (5). Here, $H_r(s)$ is a 5-th order transfer function with polynomial coefficients determined by the frequency-domain identification toolbox for radiation-force models of marine structures [38].

Thus, the right-hand side of (32) is given by

$$\frac{3.15 \times 10^{-5}s(s + 0.12)(s^2 + 1.49s + 1.48)(s^2 + 2.31s + 6.01)}{(s + 0.11)(s^2 + 1.41s + 1.33)(s^2 + 0.04s + 1.89)(s^2 + 2.36s + 5.92)}.$$

5 | RESULTS

This section presents experimental results obtained with the proposed emulator and an analysis of the overall performance of the system with the proposed control scheme.

5.1 | Experimental set-up

Here, the waves are characterized by a Bretschneider spectrum with $H_s = 0.7$ m, and $T_{av} = 6$ s. This wave condition is

FIGURE 8 Power circuit of the proposed system

FIGURE 9 Electrical machines used in the proposed system

representative of the Pecém port, where a prototype of the WEC was installed. The basic statistics of the wave climate in this area have indicated that significant wave heights are in most cases (85%) between 1 and 1.75 m, and peak period values are predominantly short, with over 55% occurrence within the narrow band from 5 to 7 s [25]. Three pumping modules are adopted for the PTO, and the PCU parameters are: $A_0 = 2 \, \text{m}^2$, $A_1 = 0.013 \text{m}^2$, $p_0 = 2 \times 10^6 \, \text{N/m}^2$, $\mathcal{V}_0 = 5.5 \, \text{m}^3$, $\rho = 1025 \, \text{kg/m}^3$, $R = 0.18 \, \text{m}$, and $H = 7 \, \text{s}$. The filter time constant τ_1 is adjusted so that $\varepsilon_{\text{filt}}$ represents the average of the piston position error for 12 s, that is $2T_{av}$.

The SCIM and DFIG are three-phase, 4 poles, 5 hp, 220 V, 60 Hz machines. The switching and sampling frequencies used are, respectively, 12 kHz and 24 kHz. The control references (21)–(24) are sent to a DSP (TMS320F28335, Texas instruments), where the generator control is implemented. Furthermore, the experimental set-up has an analogue interface card (PCI1711, Advantech) and a power circuit.

The power circuit of the experimental set-up is shown in Figure 8. A back-to-back converter (Semikron) is employed to perform the DFIG current control, which enables the decoupled control of P_s and Q_s, by adjusting, respectively, i_{rq}, and i_{rd} components, as described in Section 3.2. It is also possible to observe the GSC and RSC coupling inductors, fuses, contactors, auxiliary sources, and protection circuit breakers. The SCIM is controlled by a converter commonly used in industrial applica-
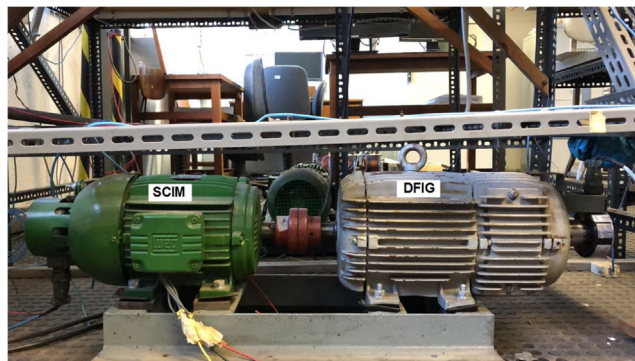
tions (CFW-09, WEG manufacturer). Despite the diode rectifier in the input stage, the four-quadrant control is possible due to the presence of a chopper circuit and a resistance in the dc link. Therefore, the energy of a regenerative braking can be conveniently dissipated in the resistance, avoiding dc link side overvoltage.

Figure 9 shows the electrical machines of the proposed system (SCIM and DFIG). Notice that both machines have the same rated power (5 hp). Ideally, a machine of higher nominal power (rating about 30 to 50% higher) would be used for the primary drive (SCIM), but due to the availability of equipment in the laboratory, machines of the same nominal power were used. This may limit the operation of the emulator, specially for the cases when the system operates at powers slightly above the DFIG nominal capacity. In such cases, the SCIM converter drive limits the torque current component to keep the rated operation powers of the machine.

5.2 | Experimental results

Figure 10 shows variables obtained with the numerical model. All variables are normalized, except f_e and δ. The IMP position (Figure 10(b)) oscillates around the reference value ($\delta_{\text{ref}} = 0$), consequently the output water flow is clearly smoothed compared to the input water flow (Figure 10(c)). The oscillations of the IMP position around the reference δ_{ref} are a consequence of the oscillating wave power filtering. During the simulation period of 200 s, a maximum IMP displacement of ± 0.2 m is observed. The limits of the IMP excursion are directly related to the HSS storage capacity.

The cross-sectional area of the water jet (A_2) and the errors (ε and $\varepsilon_{\text{filt}}$) are observed in Figure 10(d) and Figure 10(e), respectively. Around 110 and 170 s, the output water flow approaches zero to maintain the IMP position around the reference. The low energy sea drives A_2 to its minimum value. The instantaneous HSS pressure (p_1) and the velocity of the output water jet (u_2) are illustrated in Figure 10(f) and Figure 10(g), respectively. The average values of these parameters also appear in the dashed red line. The profiles are very similar to the IMP position profile, showing that with the IMP position control, the control of p_1 and u_2 are obtained intrinsically. Dynamic hydraulic
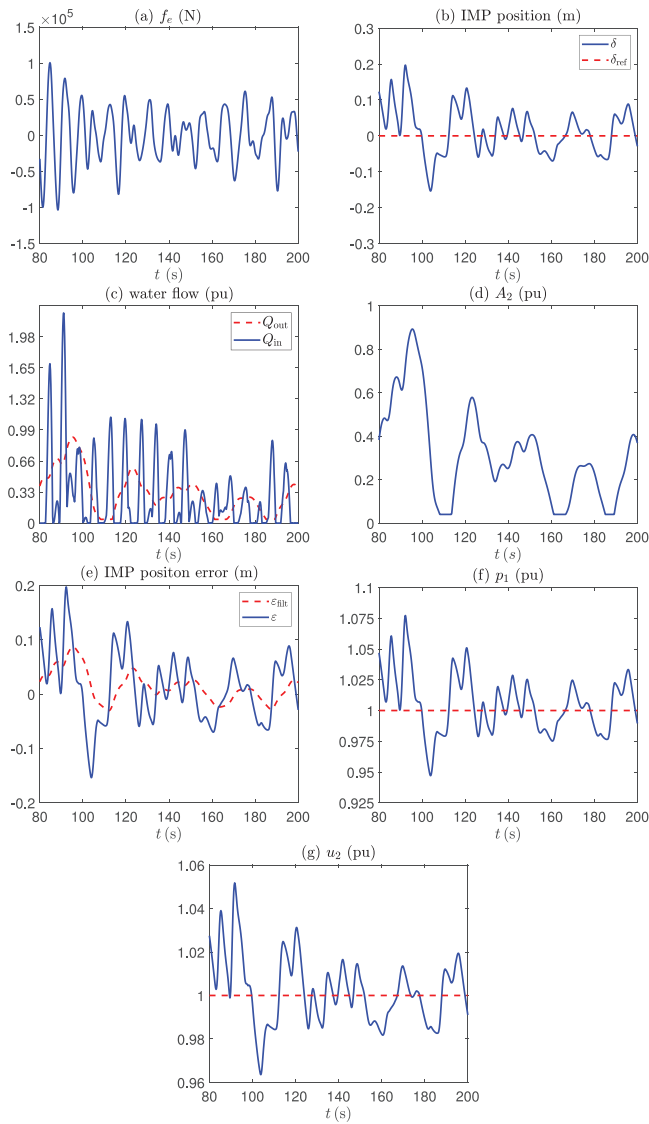
FIGURE 10 Numerical model variables: (a) excitation force (f_e), (b) IMP position (δ, δ_{ref}), (c) water flow (Q_{in}, Q_{out}), (d) water jet area (A_2), (e) IMP position error (ε, ε_{filt}), (f) HSS pressure (p_1), and (g) velocity of the water jet (u_2)

pressure control according to the sea state is of extreme importance, since the wave energy absorption is highly influenced by the hydraulic pump force f_p and, therefore, by the pressure p_1 [22]. It can be observed that p_1 oscillates around 1 pu - note that the base value for normalization is p_0, which is the optimum value for the defined sea state. Thus, the HHS pressure is oscillating around the optimum pressure.

Figure 11 illustrates the DFIG stator active power (P_s and P_{s_ref}) and the mechanical and electrical powers (P_m and P_e). Here, a certain level of filtering can be observed in P_e when compared to P_m, which results from the rotor inertia. The SCU started operation at $t = 80$ s. In fact, in the emulator startup procedure, the grid synchronization and effective DFIG connection to the grid lasted approximately 75 to 80 s. The stator active power follows the reference satisfactorily, and the generated electric power is smoothed when compared to the

mechanical power, as a result of the filtering characteristics of the rotor inertia.

Figure 12 shows that the mechanical angular speed (ω_m) follows the reference satisfactorily, except for the time interval from 85 to 105 s. A peak of electric power was generated during this interval, and the speed reference was higher than 1 pu. However, the VSC used in the SCIM drive limits the operation of the emulator because the control of the magnetizing current component must be maintained as a top priority. Thus, the control action restrains the torque current component, and causes the speed decay. In addition, the mechanical speed oscillates around the nominal speed.

5.3 | Analysis of the power conversion

Figure 13 shows the average hydraulic power absorbed by one pumping module as a function of the IMP position reference of the HSS control, for sea states with T_{av} of 6 s and different values of H_s from 0.7 to 1 m. The hydraulic power is proportional to the HSS input flow and the pressure p_1. As the theoretical power per meter of incident wavefront is proportional to the square of the significant wave heights, that is $P_w \approx 0.5 H_s^2 T_{av}$, curves with higher plateaus are observed for significant waves heights of 0.9 and 1.0 m. It can be observed that each power curve presents a maximum point of power conversion, which corresponds to the IMP position as calculated by (20). For example, when $H_s = 0.7$ m, the maximum power point is reached at $\delta_{ref} = 0$ m. Then, the HSS pressure stabilizes at values close to its optimum value of 2×10^6 N/m^2 and the average hydraulic power transferred to the HSS is about 0.08 p.u. The dotted line (δ_{opt}) highlights the evolution of maximum power points and δ_{ref} values. In general, sea states with high energy potential will operate at higher hydraulic pressures, and consequently, higher values of δ_{ref} should be adopted. For the sea states considered in this study, the efficiency of the pumping module (or the capture width ratio) is estimated in the range of 33–38%.

Figure 14 shows samples of the position profile of the floating body for different values of the IMP position reference when $H_s = 0.7$ m and $T_{av} = 6$ s. This figure illustrates how the body position is affected by the IMP position reference, which modifies the pressure of the system, and then, the PTO force (9). While with $\delta_{ref} = -0.8$ m the body moves more freely than in the other cases, with $\delta_{ref} = 0.8$ m, the motion is excessively constrained and reduces the input flow to the HSS. The optimal combination of pressure and flow results in the highest hydraulic power transferred to the HSS.

To estimate the overall efficiency of the system, the efficiencies of the hydraulic turbine and the DFIG are considered. By assuming there are six floating bodies in the system, from (17) and (18), the maximum mechanical power transferred to the shaft is 0.32 pu with an optimal mechanical speed of 0.9 p.u. (170 rad/s), as illustrated in Figure 15. Thus, an efficiency of about 70% is obtained for the turbine. In the WEC operation, it is convenient that the speed fluctuates within certain limits, as this behaviour ensures that the rotating inertia 'filters' the
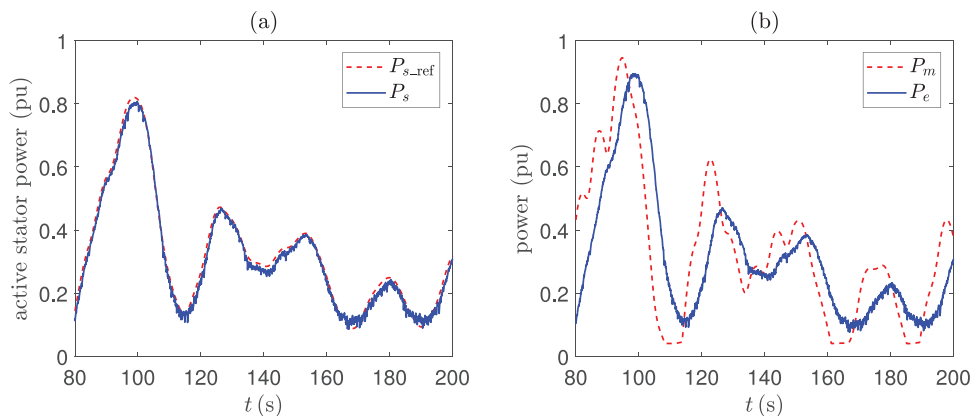
FIGURE 11   (a) Measured active DFIG stator power (P_s) and (b) mechanical power from the numerical model and estimated electrical power (P_m, P_e)
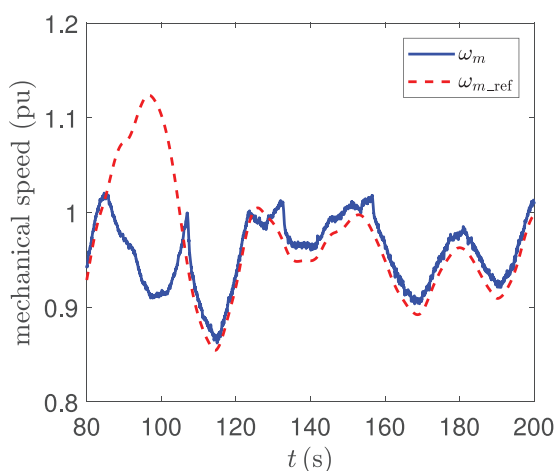

FIGURE 12   Mechanical speed of the machine. Measured speed (ω_m) and reference from numerical model (ω_{m_ref})
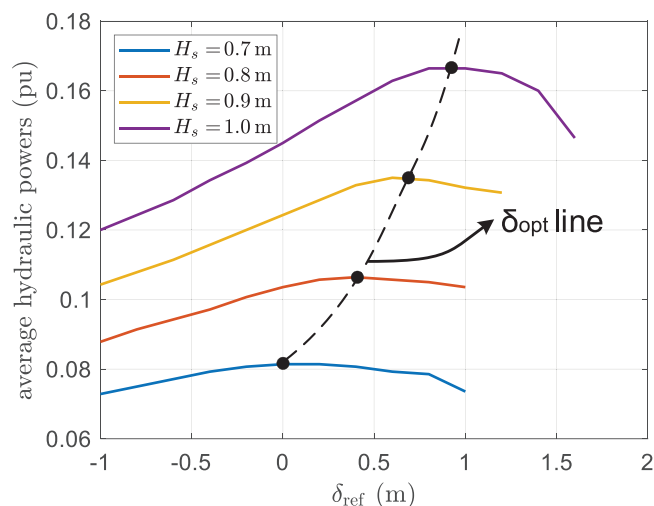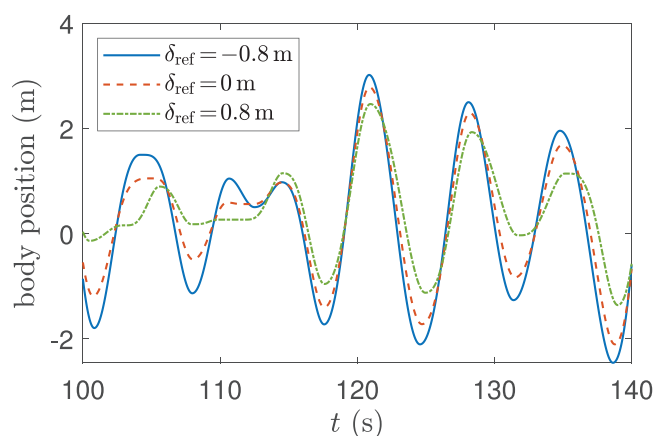

FIGURE 14   Position of the floating body for different values of the IMP position reference when $H_s = 0.7$ m and $T_{av} = 6$ s

FIGURE 13   Average hydraulic power transferred by one pumping module to the HSS versus IMP position reference

oscillating power absorbed from the waves without significant loss of efficiency. At this operating point, even if the speed varies within a $\Delta\omega$ range from 150 to 200 rad/s, the mechanical power will remain very close to the maximum mechanical power value due to the flat characteristic of the peak of the curve (Figure 15).

The variable speed operation justifies the use of the DFIG, since this machine presents excellent performance for such a type of generation system. Typically, electromechanical conversion systems have high efficiencies (above 90%) depending mainly on the machine size. Large machines (hundreds of kVA) have efficiency close to 95%, while small and medium machines have efficiencies close to 90%. In this work, the DFIG efficiency is considered as 90%. Therefore, considering the pumping module efficiency (38%), the turbine efficiency (70%) and the DFIG efficiency (90%), an overall WEC efficiency of 24% is obtained. Notice that the overall efficiency is mainly dictated by the first step of energy conversion. Thus, the control scheme that integrates both the HSS and DFIG controllers plays an important role in the overall performance of the system. If, for instance, the IMP position is different than the desired value (20), the
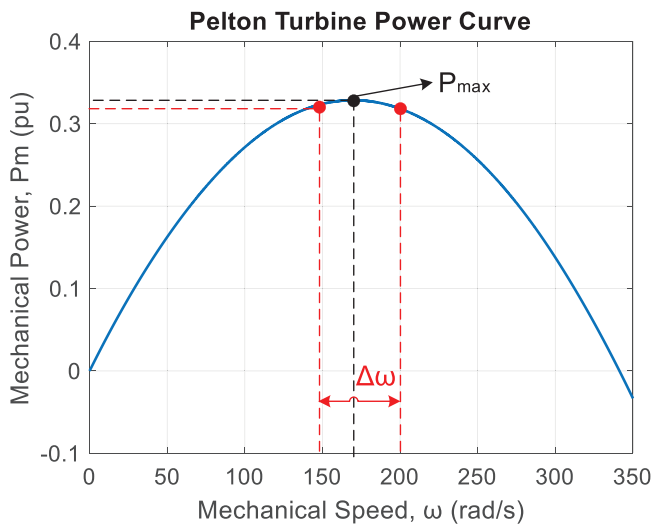
Pelton Turbine Power Curve

FIGURE 15 Typical power curve of a Pelton turbine

overall efficiency can drop up to 17% for the studied cases, assuming the same conditions for the electromechanical system.

5.4 | Discussion

The HSS control determines the active power reference for the DFIG control, allowing the integration of PCU and SCU, and the reduction of power oscillations in the power grid. The level of filtering obtained in the first stages of energy conversion can be observed in Figure 10(b) by comparing Q_{in} and Q_{out} profiles. The piston position control adopts a low-pass filter that reduces the instantaneous wave oscillations. Here, the time constant τ_1 is adjusted to filter oscillations related to the average period of the spectrum ($2T_{av}$). For cases that require higher power filtering levels, τ_1 should be increased. Larger time constants will result in greater oscillations in the IMP position.

A second power filtering stage is obtained by using the rotor inertia. The power filtering level can be observed by comparing P_m and P_e (Figure 11(b)). The power reference P_{s_ref} for the DFIG control adopts the filtered water flow output Q_{out_filt}. Here, the time constant of the filter τ_2 is also 12 s ($2T_{av}$), and the total inertia constant H is 7 s. However, higher power filtering levels require larger time constants for τ_2 (e.g. minutes or hours) and higher inertia constants (tens of seconds to minutes). In such cases, the mechanical speed variations will be higher.

6 | CONCLUSIONS

This paper presented a detailed description of a hyperbaric WEC emulator, including experimental results in a laboratory facility. The developed emulator is a very useful tool to extend the studies of the WEC in a typical setting of an electric power laboratory, and it can also be used as a guideline for the development of emulation systems for similar WECs.

In this study, the proposed hyperbaric emulation system was used for the experimental evaluation of control strategies in the primary and secondary conversion units. A control scheme that integrates the units was proposed, where the reference for active power is modified according to the available wave power in sea states. The integration of control strategies in different steps of the energy conversion process is an important step to improve the overall behaviour of the system, which has not been discussed previously.

Furthermore, the emulator also allows for the analysis of the energy storage system arrangements (HSS and mechanical inertia of the rotor). For strong grid-connections, a low storage capacity is required in both stages (HSS and rotor inertia), since the PCC voltage and frequency will be less influenced by wave power intermittencies. The oscillating wave power characteristics associated with weak grid-connections increase the storage capacities required for a secure and reliable PCC connection. Besides, when the continuity of power supply is the main control objective, as in isolated grids, the storage capacities should be increased considerably, since long storage periods are required (from the order of minutes to hours). The space available for the WEC installation is also a limiting factor for the technologies and storage levels chosen. For cases where the space limitation is critical, storage technologies with high energy densities (kWh/m^3), like the inertia of the rotor, should have preference.

The adoption of systems that emulate the behaviour of equipment that is not easily installed in laboratories (e.g. floating bodies, high-pressure hydraulic systems, large rotating inertia) contributes significantly to experimental studies related to the impact of PCU arrangements on the power grid, and the integration of control strategies applied in different steps of the energy conversion process. Factors that have a significant economic impact in wave energy systems.

This work adopted conventional PI controllers for the RSC and GSC control loops. Future works will study the performance of the hierarchical control in the event of dips and swell voltages and abnormal operating conditions in the mechanical system. Thus, other advanced control methods, for example based on robust techniques, will be incorporated in the control scheme.

ORCID
Isaac R. Machado https://orcid.org/0000-0002-8570-858X
Paula B. Garcia-Rosa https://orcid.org/0000-0002-0305-0922
Edson H. Watanabe https://orcid.org/0000-0001-6427-9504

REFERENCES
1. Wu, F., et al.: Optimal control for AWS-based wave energy conversion system. IEEE Trans. Power Syst. 24(4), 1747–1755 (2009)

2. Igic, P., et al.: Multi-megawatt offshore wave energy converters - electrical system configuration and generator control strategy. IET Renewable Power Gener. 5(1), 10–17 (2009)

3. Fusco, F., Ringwood, J.V.: A simple and effective real-time controller for wave energy converters. IEEE Trans. on Sustainable Energy 4(1), 21–30 (2013)

4. Bacelli, G., Ringwood, J.V.: Numerical optimal control of wave energy converters. IEEE Trans. on Sustainable Energy 6(2), 294–302 (2015)

5. Cantarellas, A.M., Remon, D., Rodríguez, P.: Adaptive vector control of wave energy converters. IEEE Trans. Ind. Electron. 53(3), 2382–2391 (2017)

6. Faedo, N., Olaya, S., Ringwood, J.V.: Optimal control, MPC and MPC-like algorithms for wave energy systems: An overview. IFAC J. Syst. Control 1, 37–56 (2017)

7. Garcia-Rosa, P.B., et al.: The impact of time–frequency estimation methods on the performance of wave energy converters under passive and reactive control. IEEE Trans. on Sustainable Energy 10(4), 1784–1792 (2018)

8. Mosquera, F.D., et al.: Optimal wave energy extraction for oscillating water columns using second-order sliding mode control. IET Renewable Power Gener. 14(9), 1512–1519 (2018)

9. Bjarte-Larsson, T., Falnes, J.: Laboratory experiment on heaving body with hydraulic power take-off and latching control. Ocean Eng. 33(7), 847–877 (2006)

10. Kracht, P., et al.: Performance improvement of a point absorber wave energy converter by application of an observer-based control: Results from wave tank testing. IEEE Trans. Ind. Appl. 51(4), 3426–3434 (2015)

11. Nguyen, H.-N. et al.: Experimental validation of a nonlinear MPC strategy for a wave energy converter prototype. In: Proceedings of the American Society of Mechanical Engineers (ASME) 2016, 35th International Conference on Ocean, Offshore and Arctic Engineering, Busan (2016)

12. Forbush, D. et al.: A self-tuning WEC controller for changing sea states. In: Proceddings of the 21st International Federation of Autmatic Control (IFAC) World Congress. Virtual, Online (2020)

13. Tona, P. et al.: Experimental assessment of the ifpen solution to the WEC control competition. In: Proceedings of the American Society of Mechanical Engineers (ASME) 2020. 39th International Conference on Ocean, Offshore and Arctic Engineering, Virtual, Online (2020)

14. Vermaak, R., Kamper, M.: Experimental evaluation and predictive control of an air-cored linear generator for direct-drive wave energy converters. IEEE Trans. Ind. Appl. 48(6), 1817–1826 (2012)

15. Nie, Z., et al.: Emulation and control methods for direct drive linear wave energy converters. IEEE Trans. Ind. Inf. 9(2), 790–798 (2013)

16. Ramirez, D., et al.: Emulation of an OWC ocean energy plant with PMSG and irregular wave model. IEEE Trans. on Sustainable Energy 6(4), 1515–1523 (2015)

17. Koker, K.L.D., et al.: A wave emulator for ocean wave energy, a Froude-scaled dry power take-off test setup. Renewable Energy 105, 712–721 (2017)

18. Hazra, S., Bhattacharya, S.: Modeling and emulation of a rotating paddle type wave energy converter. IEEE Trans. Energy Convers. 33(2), 594–604 (2018)

19. Estefen, S.F. et al.: Wave energy hyperbaric device for electricity production. In: Proceedings of the American Society of Mechanical Engineers (ASME) 2007. 26th International Conference on Offshore Mechanics and Arctic Engineering (OMAE), San Diego (2007)

20. Estefen, S.F. et al.: Experimental and numerical studies of the wave energy hyperbaric device for electricity production. In: Proceedings of the American Society of Mechanical Engineers (ASME) 2008. 27th International Conference on Offshore Mechanics and Arctic Engineering (OMAE), Estoril (2008)

21. Garcia-Rosa, P.B., et al.: Wave-to-wire model and energy storage analysis of an ocean wave energy hyperbaric converter. IEEE J. Oceanic Eng. 39(2), 386–397 (2014)

22. Garcia-Rosa, P.B. et al.: Efficiency optimization in a wave energy hyperbaric converter. In: Proceedings of the IEEE. International Conference on Clean Electrical Power, Capri (2009)

23. Machado, I.R., Watanabe, E.H., Garcia-Rosa, P.B.: Modeling and analysis of a sea wave energy converter. In: Proceedings of the IEEE. 13th Brazilian Power Electronics Confonference and 1st Southern Power Electronics Conference (COBEP/SPEC), Fortaleza (2015)

24. Martínez, M. et al.: Modelling and simulation of wave energy hyperbaric converter (WEHC) for applications in distributed generation. Inter. J. Hydrogen Energy 37(19), 14 945–14 950 (2012)

25. Estefen, S.F. et al.: Wave energy hyperbaric converter: Small scale models, prototype and control strategies. In: Proceedings of the American Society of Mechanical Engineers (ASME) 2012. 31th International Conference on Offshore Mechanics and Arctic Engineering (OMAE), Rio de Janeiro (2012)

26. Penalba, M., Ringwood, J.V.: A review of wave-to-wire models for wave energy converters. Energies 9(7), (2016)

27. Ochi, M.K.: Ocean Waves: The Stochastic Approach. Cambridge Ocean Technology Series 6, Cambridge University Press, New York (1998)

28. Cummins, W.E.: The impulse response function and ship motions. Schiff-stechnik 47(9), 101–109 (1962)

29. Greenhow, M., White, S.P.: Optimal heave motion of some axisymmetric wave energy devices in sinusoidal waves. Appl. Ocean Res. 19(3), 141–159 (1997)

30. White, F.M.: Fluid Mechanics, 7th ed. McGraw-Hill, New York (2011)

31. Leonhard, W.: Control of Electrical Drives, 3rd ed. Springer-Verlag, Heidelberg, (2001)

32. Pena, R., Clare, J.C., Asher, G.M.: Doubly fed induction generator using back-to-back PWM converters and its application to variable-speed wind-energy generation. IEE Proc. - Electr. Power Appl. 143(3), 231–241 (1996)

33. Pena, R., Clare, J.C., Asher, G.M.: A doubly fed induction generator using back-to-back PWM converters supplying an isolated load from a variable speed wind turbine. IEE Proc. - Electr. Power Appl. 143(5), 380–387 (1996)

34. Moreira, A.B., et al.: Power control for wind power generation and current harmonic filtering with doubly fed induction generator. Renewable Energy 107, 181–193 (2017)

35. Lima, F.K.A., et al.: Rotor voltage dynamics in the doubly fed induction generator during grid faults. IEEE Trans. Power Electron. 25(1), 118–130 (2010)

36. Luna, A., et al.: Simplified modeling of a DFIG for transient studies in wind power applications. IEEE Trans. Ind. Electron. 58(1), 9–20 (2011)

37. WAMIT, Inc.: WAMIT User Manual Versions 6.4, 6.4PC and 6.3S, 6.3S-PC, USA, 1998-2006.

38. Perez, T., Fossen, T.I.: A Matlab toolbox for parametric identification of radiation-force models of ships and offshore structures. Model. Identif. Control 30(1), 1–15 (2009)